Steering particles by breaking symmetries

Bram Bet[1,†], Sela Samin[1], Rumen Georgiev[2], Huseyin Burak Eral[2], René van Roij[1,∘]

[1]Institute for Theoretical Physics, Center for Extreme Matter and Emergent Phenomena, Utrecht University, Princetonplein 5, 3584 CC Utrecht, The Netherlands
[2]Process and Energy Department, Delft University of Technology, Delft 2628 CD, The Netherlands

E-mail: †bram.bet@gmail.com, ∘r.vanroij@uu.nl

1 March 2018

Abstract. We derive general equations of motions for highly-confined particles that perform quasi-two-dimensional motion in Hele-Shaw channels, which we solve analytically, aiming to derive design principles for self-steering particles. Based on symmetry properties of a particle, its equations of motion can be simplified, where we retrieve an earlier-known equation of motion for the orientation of dimer particles consisting of disks (Uspal *et al.*, Nature communications **4** (2013)), but know in full generality. Subsequently, these solutions are compared with particle trajectories that are obtained numerically. For mirror-symmetric particles, excellent agreement between the analytical and numerical solutions is found. For particles lacking mirror symmetry, the analytic solutions provide means to classify the motion based on particle geometry, while we find that taking the side-wall interactions into account is important to accurately describe the trajectories.

Submitted to: *J. Phys.: Condens. Matter*

1. Introduction

Micro-fluidic devices offer a vast variety of applications [1–6], where in many cases control over the position of immersed particles is offered via the channel geometry [4, 7–11] or via external fields [2, 12]. Alternatively, however, the position of the immersed particles can be controlled via the particle shape [13–16]. With techniques such as continuous-flow lithography [17], particles of quasi-two-dimensional shape can be produced in Hele-Shaw-type channels, opening possibilities to make these particle 'self-steering', following a desired trajectory.

In previous work [18], we have developed the numerical machinery to resolve the trajectories of particles that are confined in a Hele-Shaw cell, which may be of arbitrary quasi-2D shape, either by solving the hydrodynamic equations in full detail or via an effective quasi-2D description offered by the Brinkman equation. Using this framework,

we can obtain insight in the shape-dependence of the particle motion, in order to 'engineer' the trajectories, i.e. to create particles that are able to self-steer in the channel.

In this work, we gain further insight by analytically solving the equations of motion that govern the quasi-2D motion of the confined particles in Hele-Shaw channels [19, 20]. These solutions are novel and serve as a means of classification of the possible trajectories based on a few geometry-dependent parameters. Moreover, based on symmetry arguments, we rederive the angular equation of motion of a dimer-shaped particle that was earlier derived by Uspal et al. [15], but now in a general fashion by showing that it holds true for any mirror-symmetric particle.

From the analytical solutions that we construct in the wide-channel limit, we find that every particle shape admits a stable orientation in the external background flow. Independent of the initial orientation, the particle will therefore eventually align asymptotically with the stable orientation; as a result, periodic rotation cannot occur in this system unless it is due to interactions with the side walls. For mirror symmetric cases, the equations of motion simplify, allowing us to solve the transversal trajectory of the particle analytically as well.

Subsequently, we compare our analytic results with the trajectories that are obtained numerically [18]. We do this for a large variety of mirror-symmetric particles such as dimers consisting of various shapes, and symmetric trimers, and show that the motion, and its dependence on e.g. the initial orientation, is accurately captured by the analytical solution. Subsequently, we consider deviations from the mirror-symmetric shapes in a controlled fashion by considering asymmetric trimers. There, we find that the stable orientation can be tuned by varying the size ratio of the two legs of the tripod. Moreover, by varying this size ratio, the tripod particle can be focused to a non-central position along the y-axis. We find that the analytical solutions are accurate when the particle is far enough from the side walls, but that they fail to describe the motion accurately when the particle approaches the side wall, as is the case for the asymmetric trimers.

2. General equations of motion and solutions

We start by considering a solid particle of any given shape, at a position denoted by the reference point $\boldsymbol{r}_p = (x_p, y_p, z_p)$, e.g. the center of mass, in a Hele-Shaw cell, as illustrated in Fig. 1. This particle may for instance be produced using 'continuous flow lithography' [17]. Here, we will use the typical dimensions that appeared in the experiments described in our previous work [18]. The symmetry and strong confinement in the z-direction restrict the motion of the particle to the xy-plane (i.e. $z_p = 0$). Moreover, the small height H of the microfluidic device, $H \approx 30\,\mu\mathrm{m}$, combined with the typical fluid flow velocity ($U_0 \approx 50\,\mu\mathrm{m\,s^{-1}}$) and viscosity ($\eta = 55 \times 10^{-3}\,\mathrm{Pa\,s}$), imply that the Reynolds number is of the order 10^{-4} [15]. As a result, the fluid flow may be described by either the Stokes equation [21–25] or the Brinkman equation [26, 27],

both of which are supplemented with no-slip boundary conditions on the (moving) particle surface and (stationary) sidewalls, while the flow at the in- and outlet (far away from the particle) must comply with the externally imposed Hele-Shaw flow $\boldsymbol{U}_0 = \frac{3}{2}(1 - 4z^2/H^2)U_0\hat{\boldsymbol{x}}$ in the three-dimensional (Stokes) description, or $\boldsymbol{U}_0 = U_0\hat{\boldsymbol{x}}$ in the z-averaged two-dimensional Brinkman description.

Due to the linearity of the Stokes and Brinkman equations, and the overdamped nature of the particle motion and the absence of external forces, one can show [18] that the particle velocity $\boldsymbol{U}_p$ and angular velocity ω_p obey the equations of motion

$$\begin{pmatrix} \boldsymbol{F} \\ T \end{pmatrix} = -\eta\mathcal{R}\begin{pmatrix} \boldsymbol{U}_p \\ \omega_p \end{pmatrix} + \begin{pmatrix} \boldsymbol{F}_0 \\ T_0 \end{pmatrix} = \begin{pmatrix} \boldsymbol{0} \\ 0 \end{pmatrix}, \tag{1}$$

where $\boldsymbol{F} = (F_x, F_y)$ and $T = T_z$ denote the total hydrodynamic force and (the z-component of the) torque on the particle, $\boldsymbol{F}_0$ and T_0 denote the force and torque on the particle when it is held fixed subject to the externally imposed flow, and $\mathcal{R}$ is a symmetric 3×3 resistance tensor. As we have shown in [18], these quantities, and from them the force- and torque-free velocity and angular velocity, may be determined numerically from solutions to either the Stokes or the Brinkman equation, albeit with an extra term that accounts for the friction from the top and bottom plate in the latter case. However, the structure of the equation of motion (1) is identical for both formalisms, and so are the results.

The second term of the right-hand side of Eq. (1) describes the force and torque on the particle when it is held stationary in the channel, subject to the external flow $\boldsymbol{U}_0$. Invoking the argument of linearity, we derive that this term must be linear in the external flow $\boldsymbol{U}_0$:

$$\begin{pmatrix} F_{0,x} \\ F_{0,y} \\ T_0 \end{pmatrix} = \eta\mathcal{R}_0\begin{pmatrix} U_{0,x} \\ U_{0,y} \end{pmatrix}, \tag{2}$$

where $\mathcal{R}_0$ is a 3×2 tensor. Note that in the channel frame, we only consider a uniform external flow $\boldsymbol{U}_0 = (U_0, 0)$, but in the analysis below we also wish to use the particle coordinate frame, which is related to the channel frame by a rotation, such that the external flow may have both components non-zero. With this definition of $\mathcal{R}_0$, the diagonal elements of $\mathcal{R}_0$ are positive, while the sign of the off-diagonal may depend on the particle geometry and choice of particle coordinate frame.

2.1. Explicit equations of motion and solutions

Let us explicitly write out the general equations of motion for a particle moving in the channel, Eq. (1). First, we assume that we have (numerically) determined the (components of the) resistance tensors $\mathcal{R}(= \mathcal{R}_f + \mathcal{R}_w)$ and $\mathcal{R}_0$ described above, in some fixed coordinate system x', y' relative to the particle, either from the 3D or the quasi-2D description. Furthermore, let us assume that the particle is oriented with an angle θ with respect to the external background flow $U_0\hat{x}$, i.e. the coordinates x', y' differ from

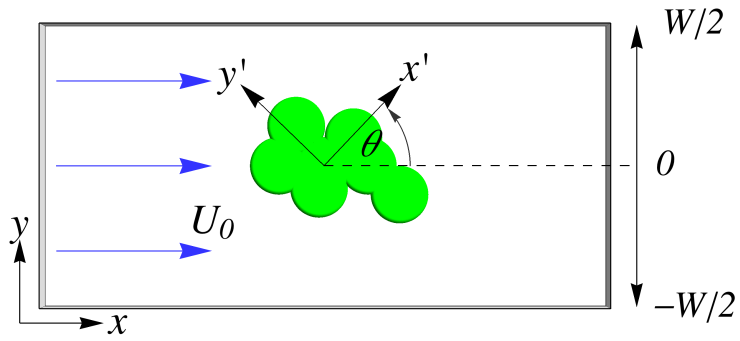

Figure 1: Geometry of a particle in a Hele-Shaw channel (top view). The lab or channel frame coordinates are denoted x, y, such that the external flow is given by $\boldsymbol{U}_0 = U_0\hat{\boldsymbol{x}}$. The particle frame is oriented at an angle θ with respect to the channel frame and has coordinates x', y'.

the lab coordinates x, y by a rotation over angle θ, as illustrated in Fig. 1. Lastly, we assume that the particle is in the center of the channel ($y = 0$), such that we can ignore any hydrodynamic interactions with the side walls for the moment.

Then, we can explicitly write out the equations of motion (1) (see Eq (A.2) in Appendix A), which can be solved to obtain the velocities $U_{p,x}, U_{p,y}$ and ω_p. The equation for θ, with $\omega_p \equiv \dot{\theta}$, has the form

$$\dot{\theta} = \frac{1}{\tau_1}\sin\theta + \frac{1}{\tau_2}\cos\theta, \tag{3}$$

where the timescales τ_1 and τ_2 are determined completely in terms of the components of $\mathcal{R}$ and $\mathcal{R}_0$ in Appendix A. Note that these τ_i may be negative. We can write the linear combination of sine and cosine in Eq. (3) as a single sine with a phase shift, Δ,

$$\dot{\theta} = \sqrt{\tau_1^{-2} + \tau_2^{-2}}\,\sin(\theta + \Delta), \tag{4}$$

where the phase shift Δ is given by

$$\Delta = \arg(1/\tau_1 + i/\tau_2). \tag{5}$$

Eq. (4) is solved by

$$\theta(t) = -\Delta + 2\arctan\left[\tan\left(\frac{\theta_0 + \Delta}{2}\right)\exp(t\sqrt{\tau_1^{-2} + \tau_2^{-2}})\right], \tag{6}$$

where $\theta_0 = \theta(0)$ is the initial orientation, see Appendix A. Recalling that $\lim_{x\to\pm\infty}\arctan = \pm\pi/2$, we find the long-time asymptotic solutions

$$\lim_{t\to\infty}\theta(t) = -\Delta \pm \pi, \tag{7}$$

where the two solutions ($\pm$) represent the same physical stationary orientation. In fact, $\theta = -\Delta$ is another stationary solution of Eq. (4), which corresponds, however, to an unstable state.

To proceed, we solve Eq. (A.2) for the transversal velocity $U_{p,y} \equiv \dot{y}$, which is written as

$$\frac{\dot{y}}{H} = \frac{1}{\tau_{y,1}} \sin^2\theta + \frac{1}{\tau_{y,2}} \sin\theta\cos\theta + \frac{1}{\tau_{y,3}} \cos^2\theta, \tag{8}$$

where explicit expressions for the timescales $\tau_{y,i} (i = 1, 2, 3)$ in terms of the components of $\mathcal{R}$ and $\mathcal{R}_0$ are again given in Appendix A. Given the solution (6), we can integrate Eq. (8) to find $y(t)$. Although this procedure does lead to a closed expression for the solution $y(t)$, this solution is too lengthy in general to provide us further insight at this point. However, we do observe from the asymptotic long-time limit of the solution (6) that we may find an asymptotic velocity $\lim_{t\to\infty} U_{p,y}(t) = U^{\infty}_{p,y} \neq 0$ in general, such that the particle persists in moving at an angle with respect to the external flow. It will therefore always enter a regime where side-wall effects ($y \sim \pm W/2$) begin to play a role.

The main conclusion we can draw from this analysis is that any particle for which τ_1^{-1} and τ_2^{-1} are not both zero, will orient asymptotically towards a stable orientation determined by the two timescales. Below, we will consider situations where we take the limit of one or both $\tau_i \to \infty$.

3. Mirror symmetric particles

The dumbbell particles described by Uspal et al. [15] and our work [18] possess an additional symmetry apart from the xy-symmetry, namely, the plane spanned by the axis connecting the centers of the two disks and the z-axis. In an unbounded fluid, the existence of this symmetry plane forces certain elements of the resistance tensor to be zero [22]:

$$\mathcal{R}_{12} = \mathcal{R}_{21} = \mathcal{R}_{13} = \mathcal{R}_{31} = 0. \tag{9}$$

This is understood as follows. Let us assume that a nonzero particle velocity U_x in the x-direction would generate a non-zero frictional force F_y in the y-direction. This system is invariant under a reflection in the x-axis, however, $F_y \to -F_y$ under this reflection, as illustrated in Fig. 2. Hence, this force $F_y = 0$ and we must conclude that $\mathcal{R}_{f,12} = \mathcal{R}_{12} = 0$.

Note that this symmetry argument assumes that the fluid around the particle is unbounded, which is only accurate if the particle is far enough from the side walls, as is for instance the case for the reorienting motion that is described in Ref [15] and [18] and below in Section 5. Finally, we can repeat this symmetry argument to find that

$$\mathcal{R}_{0,12} = \mathcal{R}_{0,21} = \mathcal{R}_{0,31} = 0. \tag{10}$$

To proceed, we assume as before that the particle, has an orientation θ with respect to the external background flow, as illustrated for the symmetric trimer particle in Fig. 3. Then, we choose an orthogonal coordinate system x', y' such that the x' axis coincides with the symmetry line of the particle.

After imposing the symmetry constraints Eqs. (9) and Eq. (10) on the resistance tensors, we can again solve Eq. (1) to obtain the particle velocities. For the angular

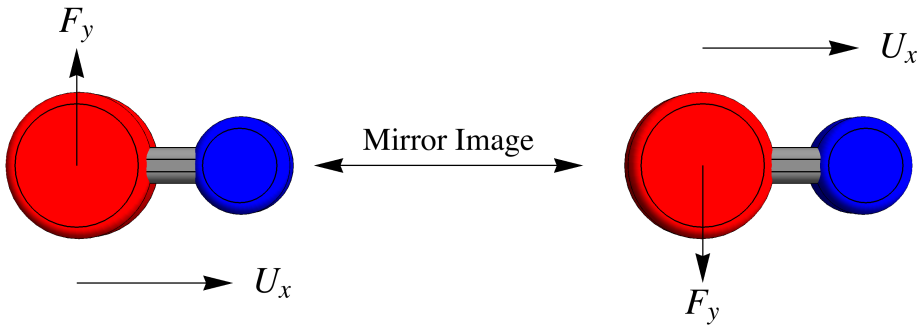

Figure 2: The system of a mirror-symmetric particle (dumbbell) translating in the x-direction. This system is invariant under reflection in the x-axis, while a non-zero force F_y in the y-direction is mapped to $-F_y$ under this reflection. Hence $F_y = 0$.

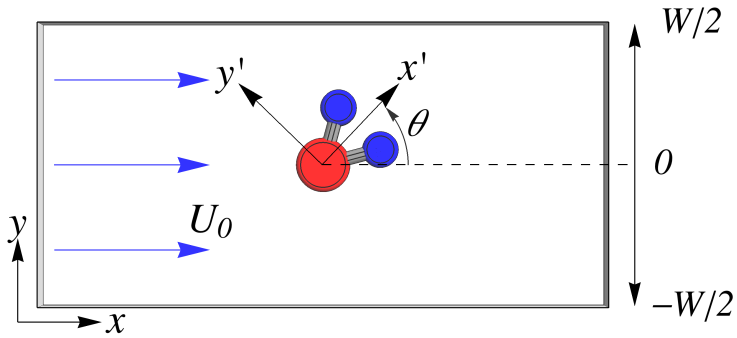

Figure 3: Geometry of a mirror symmetric particle, here a trimer or trumbbell, in a Hele-Shaw channel. As before, the lab or channel frame coordinates are denoted x, y, such that the external flow is given by $\boldsymbol{U}_0 = U_0\hat{\boldsymbol{x}}$. The particle frame is oriented at an angle θ with respect to the channel frame and has coordinates x', y'.

equation, again with $\omega_p \equiv \dot{\theta}$, we find

$$\dot{\theta} = \frac{1}{\tau}\sin\theta, \quad \text{with} \tag{11}$$

$$\tau^{-1} = U_0 \frac{R_{0,22}R_{23} - R_{0,23}R_{22}}{R_{22}R_{33} - R_{23}^2}. \tag{12}$$

Alternatively, one may obtain this equation directly from (3) by setting the appropriate components of $\mathcal{R}(= \mathcal{R}_f + \mathcal{R}_w)$ and $\mathcal{R}_0$ to zero, which in turn sets $1/\tau_2 = 0$. In that case, Eq. (5) implies $\Delta = 0 \vee \Delta = \pi$, depending on the sign of τ. Interestingly, Eq. (11) is exactly the same equation of motion for the orientation of a dumbbell as derived in [15] based on the simplification that considers only the two disks. Here, it is derived in full generality and is shown to hold for any mirror symmetric particle in the channel!

We should point out that the sign of τ depends on the choice of coordinates and origin. For instance, for the dimer particles described below, the origin was chosen in the center of the larger disk, and the equation of motion showed a negative τ. Should we have chosen to set the origin in the center of the smaller disk for instance, then the

off-diagonal terms in $\mathcal{R}$ and $\mathcal{R}_0$ will change sign, such that τ becomes positive, leading to an asymptotic orientation $\theta = \pi$, which now corresponds to the larger disk behind, as one would expect.

Eq. (11) can be solved to give

$$\theta(t) = 2\arctan\left[\tan(\theta_0/2)e^{t/\tau}\right], \tag{13}$$

which can be obtained from Eq. (6) by setting $\Delta = 0$ or $\Delta = \pi$, depending on the sign of τ. As before, $\theta_0 = \theta(0)$ denotes the initial orientation at time $t = 0$. Furthermore, we can solve for the velocity in the y-direction:

$$\begin{aligned} U_{p,y} &= U_0 \cos\theta \sin\theta \\ &\quad \times \frac{R_{0,23}R_{11}R_{23} - R_{0,22}R_{11}R_{33} + R_{0,11}(R_{22}R_{33} - R_{23}^2)}{R_{11}(R_{22}R_{33} - R_{23}^2)}, \end{aligned} \tag{14}$$

which we may write, with $U_{p,y} = \dot{y}$, as

$$\frac{\dot{y}}{H} = \frac{U_{p,y}}{H} = \frac{1}{\tau_y}\sin 2\theta. \tag{15}$$

Given the solution (13), we can integrate Eq. (15) to find

$$\frac{y(t)}{H} = \frac{2\tau \sin\theta_0}{\tau_y}\left(\frac{1}{\cosh(t/\tau) + \sinh(t/\tau)\cos\theta_0} - 1\right), \tag{16}$$

where we assumed the initial position to be $y(0) = 0$. Details are given in Appendix A.

3.1. Asymptotic behaviour, zeros and critical points

From (13) we can investigate the asymptotic orientation of mirror-symmetric particles by taking the limit $t \to \infty$. Depending on the sign of τ (which depends on the particle geometry), we find

$$\lim_{t\to\infty} \theta(t) = 0 \vee \pi, \tag{17}$$

which is in agreement with setting $\dot{\theta} = 0$ in (11). The asymptotic y-position is easily seen to be $y/H = -2\tau \sin\theta_0/\tau_y$. Also, by finding the roots of the solution (16), we can determine where the particle crosses the x-axis, which occurs at time $t/\tau = 0$ (since we set $y(0) = 0$ as mentioned below solution (16)), or at $t_c/\tau = \log\frac{1-\cos\theta_0}{1+\cos\theta_0}$, if $|\theta_0| > \pi/2$. Furthermore, for $|\theta_0| > \pi/2$, we can derive that the particle reaches the maximum transversal amplitude $y(t_m/\tau) = \frac{2\tau}{\tau_y}(1 - \sin\theta_0)$ at time $t_m = t_c/2$. Note that this precisely corresponds to $\theta(t_m) = \pi/2$, which is easily seen from Eq. (15) as the right-hand-side changes sign for $\theta = \pi/2$. Details of these derivations are given in Appendix A.

These results show that the motion of mirror-symmetric particles is completely characterised by the initial orientation θ_0 and the time scales τ and τ_y, which in turn are determined by the particle geometry. The analytical solutions provide us a recipe to directly tune the particle trajectories by varying these geometric parameters or initial conditions.

4. Particles with two symmetry axes

Finally, we consider the case that the particle has yet another axis of mirror symmetry which is perpendicular to the symmetry axis described above. For convenience, we take this axis to be the y' axis in the particle frame, and choose the origin in the intersection of these two axes. Using the same arguments based on mirror symmetry as before [22], we find that $\mathcal{R}$ is diagonal in this case. Similar arguments then give us that $\mathcal{R}_{0,32} = 0$. Writing down Eq. (1) explicitly again and solving for the angular velocity, we find that the rotational motion completely decouples from the translation, as we find $\dot{\theta} = \omega_p = 0$, since the off-diagonal resistance components vanish. Alternatively, one can obtain this from (11) by setting the appropriate components of $\mathcal{R}$ to zero, to find $1/\tau = 0$. Hence, the particle will not rotate at all and every orientation is stable. Interestingly, the particle will still move in the transversal direction, as this velocity is solved by

$$\dot{y} = U_{p,y} = U_0 \frac{R_{0,11}R_{22} - R_{0,22}R_{11}}{R_{11}R_{22}} \cos\theta \sin\theta \tag{18}$$

Hence, for $\theta \neq k\pi/2$ with integer k, we find that the particle moves transversely. Examples of shapes with two axes of symmetries are rods or the symmetric dumbbells considered by Uspal et al. [15]. They observed indeed that the symmetric dumbbells move transversely in the channel without rotating. This motion is continued until the dumbbells are reflected by the side walls (that are not incorporated in this analysis).

Note that if the particle has fourfold symmetry, i.e. the shape is invariant under a rotation by $\pi/2$, then this will force $R_{11} = R_{22}$ and $R_{0,11} = R_{0,22}$, setting $U_{p,y} = 0$. In other words, the transversal motion in (18) is directly related to the mismatch in resistance coefficients: $R_{11} \neq R_{22}$, a remark often made in the literature, in the context of slender-body theory and in the description of for instance sedimentation of rod-like particles [23].

5. Comparison with numerical results

After having established the analytical results of Sections 2 and 3, we now compare these to numerical and experimental data. The agreement or disagreement of our analytical results with the numerically obtained trajectories will provide us information about the assumptions we made in the derivations above, such as ignoring the influence from the side walls.

Below, we will stick to the experimental dimensions of Ref. [15] as much as possible. Specifically, the channel height $H = 30\,\mu\text{m}$ is taken as a unit of length; the experimental channel width $W = 500\,\mu\text{m}$ is therefore set at $W/H = 16.67$, unless specifically mentioned otherwise. The particle height corresponds to a gap $h/H = 0.06$ between the particle and top and bottom wall. Moreover, we consider composite particles consisting of disks or other shapes, of typical size R_i (usually disk radius), connected by cuboid parts of length $s/H = 2.09$ and width $w/H = 0.456$. The size ratios R_i/R_j will be

varied below, while the smallest size is fixed at $R_i/H = 0.625$ (the choice of i depends on the specific particle geometry, as will become clear below).

5.1. Mirror symmetric particles

We have considered a large variety of mirror symmetric shapes that can be fabricated with continuous flow lithography. Specially, next to the earlier-considered dimers of disks with different radii, we have investigated the behavior of dimers consisting of triangles and squares, of different aspect ratios R_1/R_2, where these radii refer to the radii of circumscribed disks. Also, we have investigated trimer (or trumbbell) particles, consisting of three connected disks of similar dimensions as the earlier considered dumbbells, where the middle disk has a larger radius $R_2 > R_1 = R_3$, as illustrated in Fig. 3. The angle between the two legs is denoted by ϕ, as shown in Fig. 8.

The mirror symmetric shapes described here all have in common that one of the parts of the dimer, or the middle disk of the trimer, is larger than the other part. Choosing the origin of the particle frame in the center of the larger part (as we have done before in the case of the disk dimers), it is easy to see that the nonzero off-diagonal elements of $\mathcal{R}$ must be negative: translation in the positive y-direction will generate a positive torque (corresponding to a counterclockwise rotation) and vice versa. Similarly, an external flow in the y-direction (in the particle frame) will generate a negative torque (hence clockwise rotation). Taking this together, we conclude that all these shapes obey Eq. (11) with a negative sign, such that they orient in the external flow with the larger part behind. Hence, all these shapes will show a qualitatively identical trajectory, fully characterized by the geometry-dependent timescale τ that is to be determined numerically. In Fig. 4, we illustrate this point by showing snapshots of the reorienting motion of different shapes with different size ratios at different times t/τ. We show:

(a) a dimer of squares with aligned edges (which we define as type I) and $R_1/R_2 = 1.25$, at $t/\tau = 0$;

(b) a dimer of squares with aligned diagonals (def. type II) and $R_1/R_2 = 1.5$), at $t/\tau = 1$;

(c) a dimer of triangles with aligned edges (def. type I) and $R_1/R_2 = 1.75$, at $t/\tau = 2$;

(d) a dimer of triangles with the triangles pointing towards each other (def. type II) and $R_1/R_2 = 2.0$, at $t/\tau = 3$;

(e) a trimer of disks with $R_1/R_2 = R_3/R_2 = 1.5$ and $\phi = 50°$ at $t/\tau = 4$; and

(f) a dimer of disks with $R_1/R_2 = 3.0$, at $t/\tau = 5$.

Around the particles, we show in Fig. 4 isobars of the disturbance pressure field $p-p_0(x)$ created by the particle, with p_0 the pressure field corresponding to an undisturbed external flow U_0 in the channel, i.e., $p_0(x) = (x - L/2)\nabla p$, $-L/2 < x < L/2$, with L the length of the channel, such that $U_0 = -H^2\nabla p/(12\eta)$.

In Fig. 5, we plot the orientation θ as a function of rescaled time t/τ, for the different shapes illustrated in Fig. 4. Indeed, we clearly observe that the angular motion

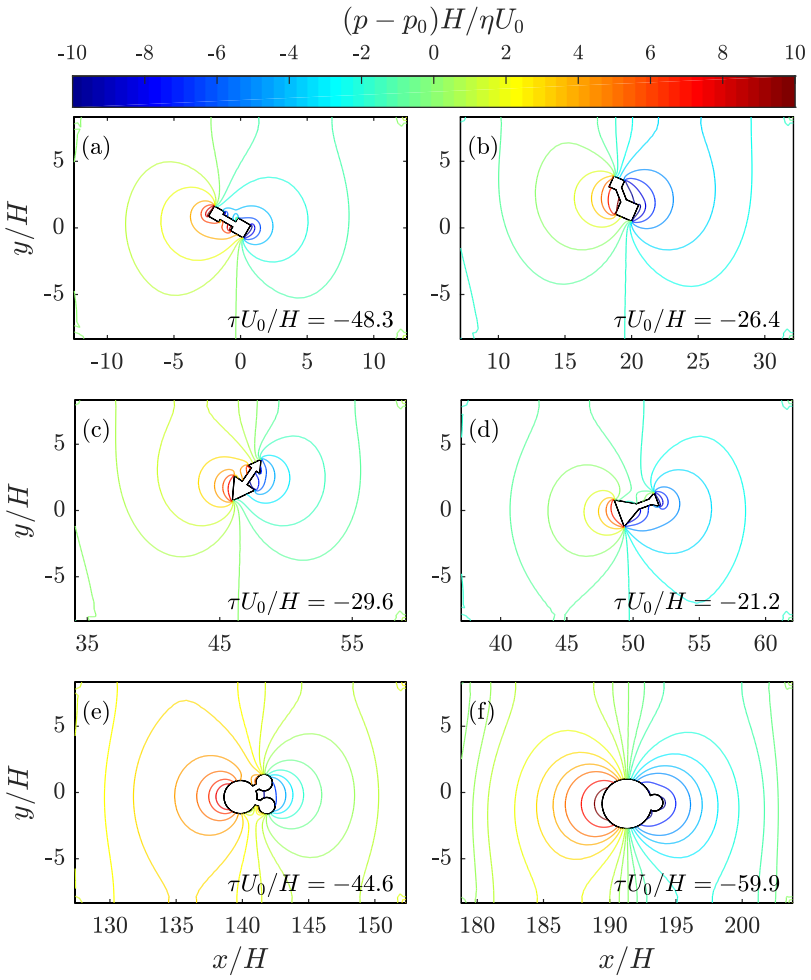

Figure 4: Snapshots of isobars of the disturbance pressure field around different mirror symmetric particles in the micro-fluidic channel, all performing a qualitatively similar reorienting motion. Shown are (a) a dimer consisting of: two squares with one edge parallel and $R_1/R_2 = 1.25$ at $t/\tau = 0$, (b) two squares with diagonals parallel and $R_1/R_2 = 1.5$ at $t/\tau = 1$, (c) two triangles with one edge parallel and $R_1/R_2 = 1.75$ at $t/\tau = 2$, (d) two triangles pointing towards each other with $R_1/R_2 = 2.0$ at $t/\tau = 3$. Here, the radii correspond to the radius of a circumscribed disk. Moreover, we show (e) a trimer with $R_1/R_2 = R_3/R_2 = 1.5$ and opening angle $\phi = 50°$ at $t/\tau = 4$, and (f) a dumbbell with $R_1/R_2 = 3.0$ at $t/\tau = 5$.

is perfectly described by the solution (13), as all the data collapse on the analytical curve once time is rescaled by τ (which differs for each shape). Moreover, we compare our analytical results for the motion in the y-direction with the numerically obtained trajectories in Fig. 6, where we rescaled the position by a factor τ_y/τ, and find that the data collapse on the analytical solution. In particular, this confirms that our analytical results for the time and height of the maximum and the time for which $y = 0$ are correct. We observe that initially, the particles move in the direction opposite to their final position: $\dot{y}(t < t_m) > 0$, while $\dot{y}(t > t_m) < 0$, as was already noted in Section

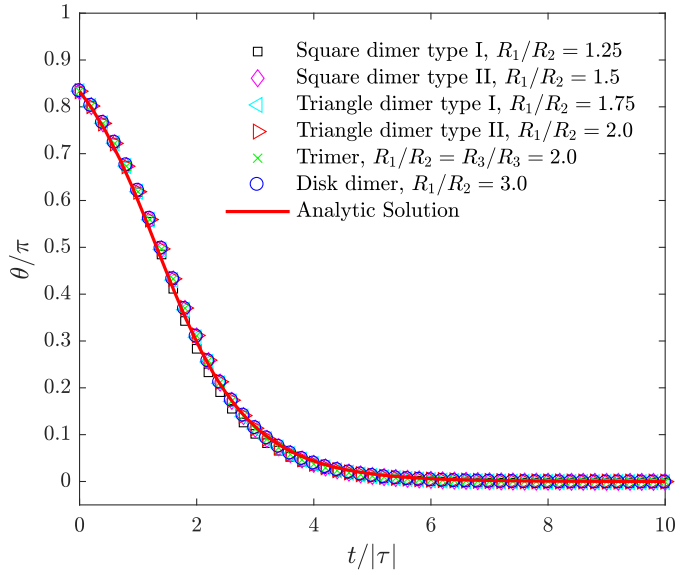

Figure 5: Orientation θ as a function of rescaled time t/τ, for the different shapes illustrated in Fig. 4, all starting with $\theta(0) = 5\pi/6$.

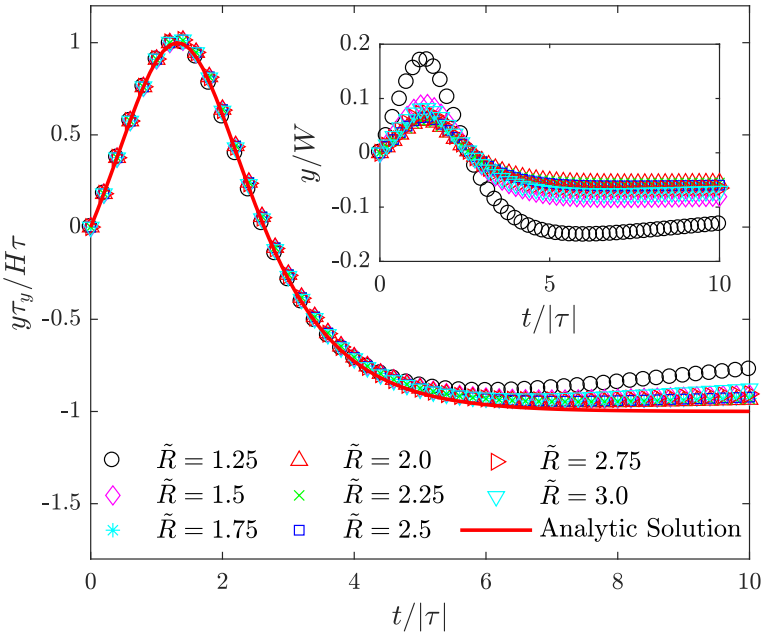

Figure 6: The transversal trajectories $y(t)$, rescaled by the two geometry-dependent timescales τ/τ_y, that appear in the Eq. (11) and Eq. (15), for disk dimers of varying shape parameter $\tilde{R} = R_1/R_2$. In the inset we show another scaling of the y-position in units of the channel width W, as a function of time.

3.1. We can compare this qualitatively to the sedimenting rod example, mentioned in section 4, which moves upwards when $\pi/2 < \theta < \pi$, and downwards when $0 < \theta < \pi/2$. As an example, an animation of the motion of a triangle trimer can be found in the supplementary material (Appendix B).

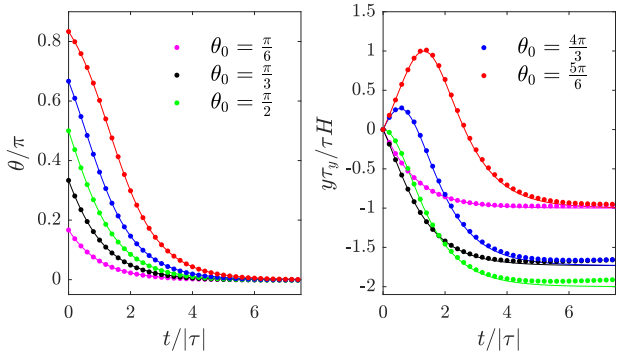

Figure 7: The orientation θ (a) and y-coordinate (b) as a function of time t/τ, for a disk dimer particle with $R_1/R_2 = 2.0$, for different initial angles θ_0. The points show the numerically integrated trajectories, while the solid lines show the analytical solutions. In all cases, $y(0) = 0$.

At a later stage of the trajectory ($t > 5\tau$), we see a deviation from the analytical curve that is caused by hydrodynamic interactions with the sidewall of the channel. This effect is more pronounced for $R_1/R_2 = 1.25$, since this shape moves further from the channel center and closer to the sidewall, as can be see in the inset of Fig. 6, where we show the position y relative to the channel width W, as a function of time.

Next, we investigate the dependence of the solutions (13) and (16) on the initial angle θ_0. The results are shown in Fig. 7, where we show the orientation θ (Fig. 7(a)) and the y-position (Fig. 7(b)) as a function of time, for a disk dimer with $R_1/R_2 = 2.0$. The data points are obtained by numerical integration of Eq. (1), while the analytic solutions are shown by the solid lines. We observe perfect agreement between the two results. Only for later times, we observe again that the interaction with the side walls will push the particle slowly towards the center of the channel ($y = 0$).

Interestingly, we can influence the direction and magnitude of the y-motion by varying the particle shape. Specifically, for the symmetric trimers, we find that the timescale τ_y can change sign when the angle ϕ between the legs is varied. In Fig. 8, we show the timescales τ (red) en τ_y (blue) as a function of ϕ, for a trimer particle consisting of three disks with ratios $R_2/R_3 = R_2/R_1 = 1.5$, R_2 being the ratio of the larger middle disk. Fig. 8 shows that τ_y is discontinuous and changes sign around $\phi = 60°$. This can also be seen in Fig. 9, where the y-position as a function of time t is shown, for trimers with different opening angles ϕ. We observe that for $\phi < 60°$, the particles first move in the positive y-direction to a maximum $y(t_m)/H = \frac{2\tau}{\tau_y}(1 - \sin\theta_0) > 0$ at $t_m/\tau = \frac{1}{2}\log\frac{1-\cos\theta_0}{1+\cos\theta_0}$, as determined above, and subsequently cross $y = 0$ to reach an asymptotic position $y = -\tau/\tau_y < 0$. For $\phi > 60°$, this motion is precisely reversed: $y(t_m) < 0$ and an asymptotic position $y/H = \tau/\tau_y > 0$. For $\phi = 60°$, we observe almost no transversal motion, consistent with $\tau_y^{-1} \approx 0$. In the inset of Fig. 9, we show the position y rescaled by τ/τ_y, for the trimers with different opening angles ($\phi = 60°$ excluded), and observe that the data collapse on the analytical solution (16). Finally,

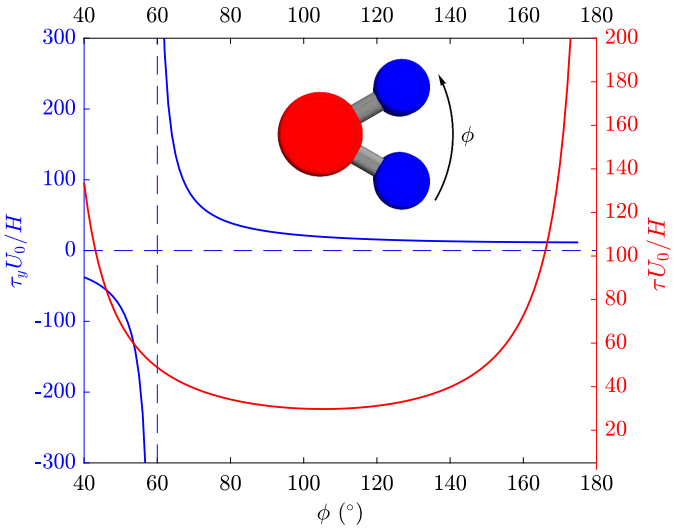

Figure 8: The timescales τ_y (blue) and τ (red) as a function of the angle ϕ between the legs of the trimer, with $R_2/R_1 = R_2/R_3 = 1.5$.

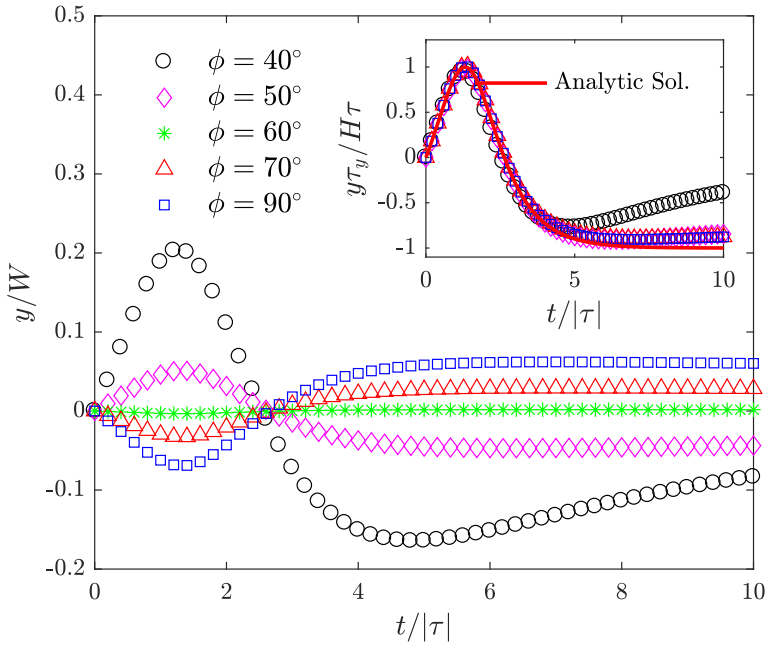

Figure 9: The transversal position y (in units of the channel width W), as a function of time t/τ, for trimers of varying opening angle ϕ, starting at $y(0) = 0$ and $\theta(0) = 5\pi/6$. In the inset we show $y(t)$ ($\phi = 60°$ excluded) but rescaled by $H\tau/\tau_y$.

we point out again that we observe that interactions with the side walls will eventually push the particles towards the center of the channel.

5.2. Broken mirror symmetry

All particle shapes we have considered so far possess a mirror symmetry, which forces them to a stable orientation of $\theta = 0$ or $\theta = \pi$ and a terminal velocity that is parallel to the external flow, albeit with a slow motion in the direction of the center of the channel due to the interaction with the side walls. This means that if we are interested in steering the particles away from the center, we should break the mirror-symmetry. In this section, we break the mirror symmetry in a controlled fashion by considering asymmetric trimer particles, in which the disk at one of the legs is larger than the other. To be specific, we fix $R_2/R_3 = 2.0$ and $\phi = 50^\circ$ and vary R_1/R_3. With $R_2 > R_1, R_3$, we still expect the particle to orient with the larger disk behind, but since $R_1 > R_3$ we will have $1/\tau_2 \neq 0$, which implies (as is seen from Eq. (6)) that $\theta(\rightarrow \infty) \neq 0$. We point out that for shapes with $R_1/R_3 > 1.8$, a small area (of fluid) is enclosed between the three disks of the dimer, which leads to instabilities in our numerical calculations. Therefore, we will only consider shapes with $1 < R_1/R_3 \leq 1.8$ for now.

In order to compare with our analytical solutions, we first consider the case without side wall interactions, i.e., we make the channel very large compared to the particle by setting $W/H = 200$. In Fig. 10, we show the orientation θ as a function of time, for the different trimer shapes. The data points indicate the numerically solved trajectories from Eq. (1), and the solid lines show the analytical solution, with the timescales τ_1 and τ_2 obtained numerically from Eq. (3). We observe perfect agreement between the two results. Moreover, we clearly observe that for increasing R_1/R_3, the asymptotic orientation $\theta(t \rightarrow \infty)$ increases and deviates from 0, as is also shown in the inset of Fig. 10.

In turn, the non-zero angle in the long-time limit has an effect on the transversal motion, which is shown in Fig. 11 for the trimer particles. Initially, the particles show motion qualitatively similar to the mirror-symmetric case, with a positive peak $y_m > 0$ and crossing $y = 0$ at some later time. However, rather than a constant asymptotic position, the particles attain a negative asymptotic velocity such that $y(t \rightarrow \infty) = -\infty$ in the case where $W \rightarrow \infty$. Even without knowing all three $\tau_{y,i}$ in Eq. (8), we can already gain some insight by comparing with the mirror-symmetric case. The fact that we have a maximum $y(t_m) > 0$ implies that $\tau_{y,2} < 0$ and either $\tau_{y,1}, \tau_{y,3} < 0$ or $|\tau_{y,1}|, |\tau_{y,3}| < |\tau_{y,2}|$. Then, as $\theta(t \rightarrow \infty) > 0$, we find that $U_{p,y}(t \rightarrow \infty) < 0$.

These results change when the side wall interactions are taken into account. In Fig. 12, we show the orientation of trimer particles with different R_1/R_3, with the original channel dimensions ($W/H = 16.7$). Let us first discuss the shapes with $1 \leq R_1/R_3 \leq 1.6$. For these shapes we find that, initially, the reorientation is correctly described by the analytical solutions, although a deviation occurs due to sidewall effects. Specifically, we observe that the long-time limit of θ is negative for each particle (except for the symmetric particle with $R_1/R_3 = 1.0$), whereas we expect a positive asymptotic orientation from the analytic solutions. Recall that the fluid moves slower close to the no-slip side-walls, leading to a clockwise rotation when the particle is close to the

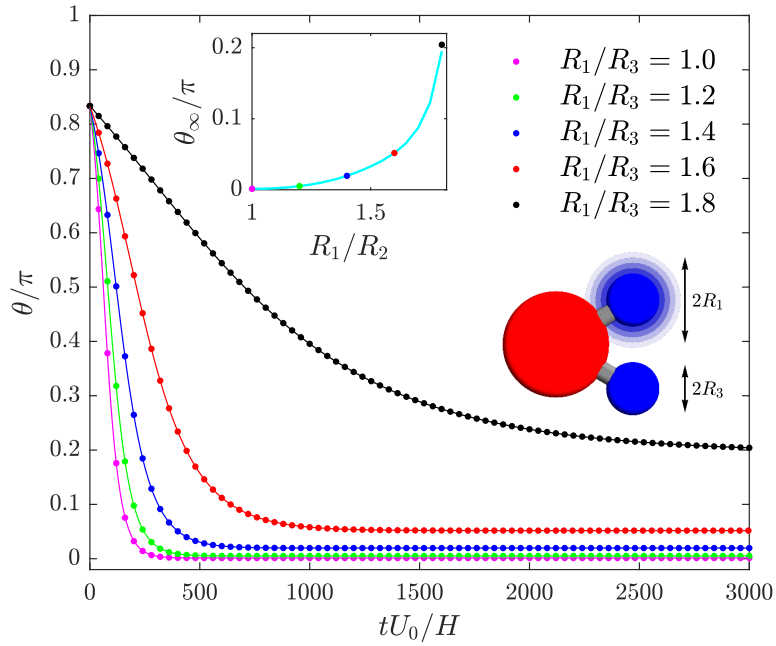

Figure 10: The orientation θ as a function of time t, for trimer particles with $R_2/R_3 = 2.0$, $\phi = 50°$ and varying R_1/R_3. The initial orientation is $\theta_0 = 5\pi/6$. The points show the numerically obtained trajectories and the solid lines show the analytical solutions. Here, the channel side walls are placed at $y = \pm W/2 = \pm 100H$. The inset shows the long-time limit orientation $\theta_\infty = \theta(t \to \infty)$.

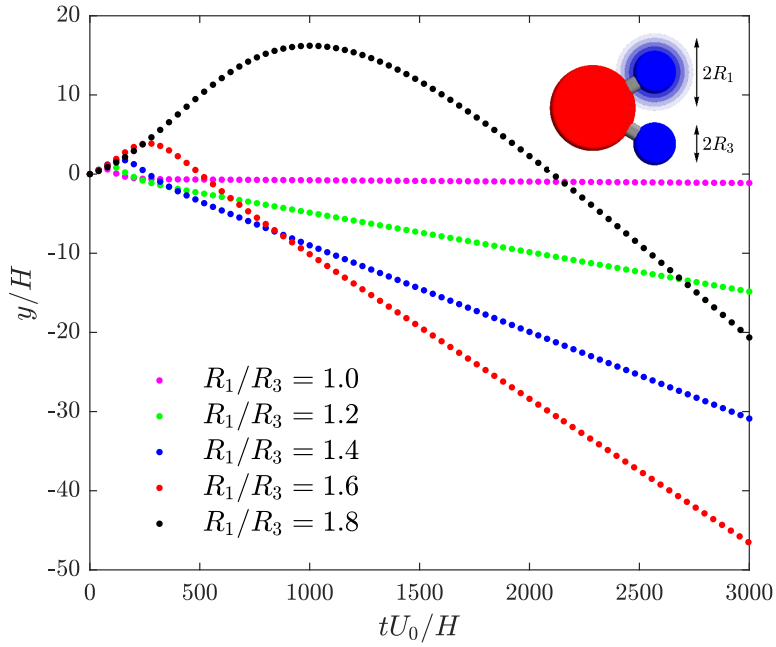

Figure 11: The transversal position y as a function of time t, for trimer particles with $R_2/R_3 = 2.0$, $\phi = 50$ degrees and varying R_1/R_3. The initial orientation is $\theta_0 = 5\pi/6$ and the initial position is $y(0) = 0$. Here, the channel side walls are placed at $y = \pm W/2 = \pm 100H$.

lower side wall at $y = -W/2$. Thus, we observe that a competition between the shape-determined asymptotic orientation (which is positive) and the side-wall effects (rotating the particle clockwise), leads to a stable orientation, which is negative.

For $R_1/R_3 \geq 1.65$, the interactions with the side walls lead to very different (and complicated) trajectories. Initially, we see that the particles reorient according to the analytical solution, as is also observed in the inset of Fig. 12, where we show an enlarged plot of the $\theta(t)$ data for $0 < tU_0/H < 400$. However, at a later time ($tU_0/H \approx 300$), the particle moves very close to the upper side wall at $y = W/2$ (see also Fig. 13), causing the particle to reverse its rotation. The no-slip boundary condition on the side wall, $\boldsymbol{u}(y = W/2) = 0$, forces the fluid velocity to be low near this side wall, while the fluid velocity away from the side wall is much larger, naturally leading to a rapid counterclockwise rotation of the particle near this side wall. Subsequently, for the shapes with $1.65 \leq R_1/R_3 \leq 1.75$ we observe a slower reorientation determined by a complicated interplay of their shape-determined reorientation and the side-wall interactions. In the long-time limit, these shapes reach a negative stationary stable orientation, similar to the shapes $R_1/R_3 \leq 1.6$. The trajectory of $R_1/R_3 = 1.8$ is even more complicated, as another rapid reorientation (clockwise) is observed at $tU_0/H \approx 800$. Subsequently, the particle qualitatively performs the reorienting motion as dictated by its shape, after which another encounter with the side wall at $y = -W/2$ at $tU_0/H \approx 2000$ rotates the particle clockwise (see also Fig. 13).

In Fig. 13, we show the transversal position y as a function of t for the different trimer particles, again for $W/H = 16.7$. For $1.2 \leq R_1/R_3 \leq 1.6$, we clearly observe that the particles move to the lower half of the channel ($y < 0$) at later times ($t > t_c$, in the notation of Section 3.1). This is consistent with our findings without the effects from the side walls, as shown in Fig. 11. However, in the long-time limit, the particles move parallel to the side wall. Clearly, a competition between the effects of a negative transversal velocity once the stable orientation is attained, and the repulsive hydrodynamic interaction with the sidewalls, forces the particles to move at a fixed distance from the side walls. This is also true for the particles with $1.65 \leq R_1/R_3 \leq 1.75$, for which we observe a stable position in the long-time limit, after a period of oscillating motion due to the interplay between the shape-determined motion and side-wall effects. For $R_1/R_3 = 1.8$, we observe even more oscillations, as the particle moves very close to the side walls at times $tU_0/H \approx 300, 800$ and 2000, where a rapid counterclockwise reorienting motion takes place as we observed in Fig. 12. Due to this reorientation, the particle acquires a large transversal velocity, such that it moves to the other side wall where another reorientation takes place. This motion is in fact very similar to the oscillating motion of the symmetric dumbbell particles discussed in Ref. [15], which do not rotate due to shape, but do acquire a transversal velocity (see Section 4). However, after a long time $tU_0/H \approx 6000$ (not shown) also this shape attains a stable orientation and y-position. This is shown more clearly in Fig. 14, where we show the particle trajectory in the (θ, y) phase space, where time is running along the curves as indicated by the arrows. There, we clearly see that all shapes with $R_1/R_3 > 1$ will move to a

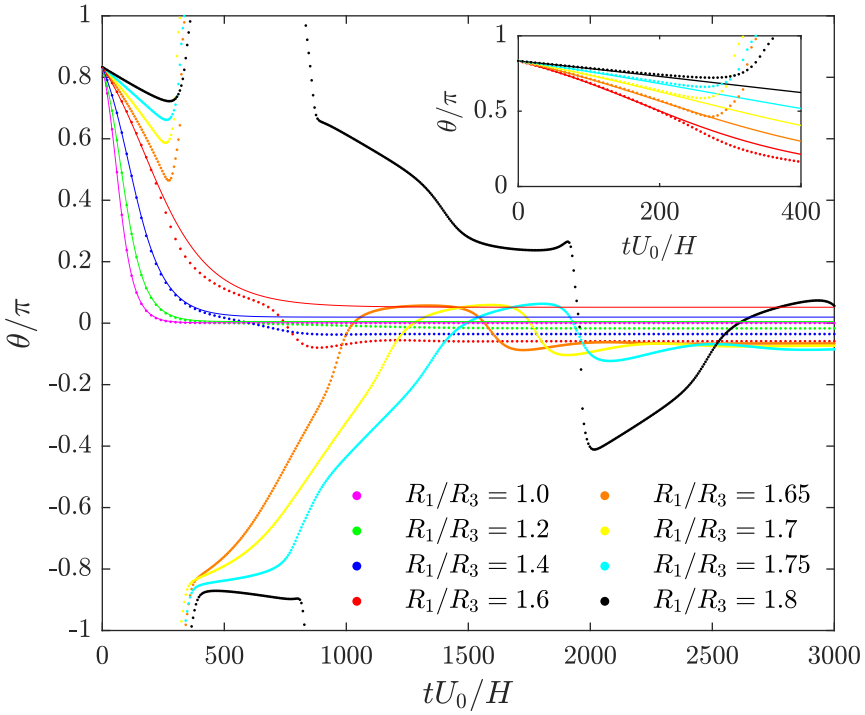

Figure 12: The orientation θ as a function of time t, for trimer particles of varying size ratio R_1/R_3, with $R_2/R_3 = 2.0$ and $\phi = 50°$, for a channel width $W/H = 16.7$ (that matches the experiments of Ref [15]). Here, $\theta(0) = 5\pi/6$ and $y(0) = 0$. The points show the numerically obtained particle trajectories, the solid lines show the analytical solutions. In the inset, the numerical and analytical curves of $\theta(t)$ are enlarged for $0 < tU_0/H < 400$, for the trimers with $R_1/R_3 \geq 1.6$.

stable position $y \approx -0.3W$ at a slightly negative angle in the long-time limit, while the symmetric trimer ($R_1 = R_3$) attains a limit orientation $\theta \approx 0$ and a y-position close to the center at $y = 0$. Animations of the motion of a few of these trimer particles can be found in the supplementary material (see Appendix B).

Thus, we have observed that the presence of side walls strongly affects the motion for these asymmetric particles. However, our analytical solutions can still provide a qualitatively prediction of the motion: the particles with $1 < R_1/R_3 \leq 1.8$ will all move to the lower half of the channel ($y < 0$), consistent with the analysis without side walls. In fact, when we consider particles with $R_3 > R_1$, our previous analysis immediately gives us that the trajectories will be the mirror image of Fig. 13: these particles will move towards $y > 0$, in which case the side wall interaction will lead them to move parallel and close to the upper side wall (at $y = W/2$). We summarize these conclusions in a 'state diagram' in Fig. 15, which, with the goal of engineering trajectories in mind, can be read a set of preliminary 'design rules'. There, the black lines indicate symmetric particles with $R_1 = R_2$ (symmetric dimers), $R_1 = 0$ or $R_3 = 0$ (symmetric dimers) that move to the center of the channel, while the red and blue areas indicate shapes with a long-time y-position that is close to the lower ($y = -W/2$) and upper ($y = W/2$)

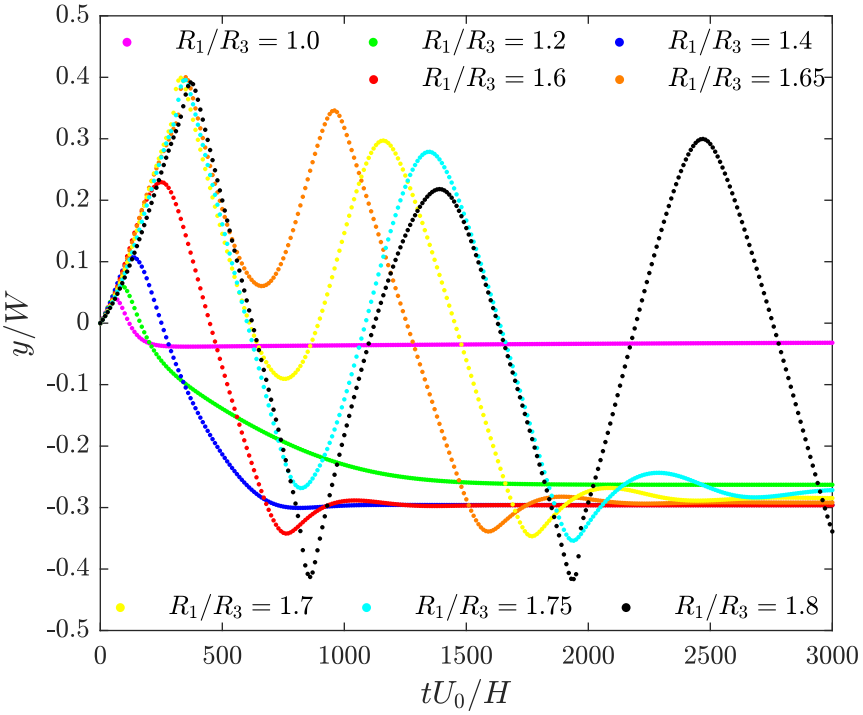

Figure 13: The transversal position y as a function of time t, for trimer particles of varying size ratio R_1/R_3, with $R_2/R_3 = 2.0$ and $\phi = 50°$ and channel width of $W/H = 16.7$. The data is obtained from numerically solving the particle trajectories. As before, $\theta(0) = 5\pi/6$ and $y(0) = 0$.

boundary, respectively. More research is needed to complete this diagram in the future.

6. Summary and Outlook

We have derived analytical solutions to the equation of motion of general particles that undergo strongly confined quasi-2D motion in Hele-Shaw cells. Making use of symmetry arguments, these equations were simplified and the angular differential equation from Ref. [15] is recovered, not only for dimers of disks but in fact even for any particle with a mirror symmetry. Our analytical solutions were compared extensively with the numerically obtained trajectories, and excellent agreement between these results was found. With these analytical results, we are able to fully predict the particle trajectories of any mirror-symmetric shaped particle, by only determining the two geometry-dependent time-scales τ and τ_y that follow from the resistance tensor. For non-symmetric shapes, we also found excellent agreement, where we found that asymmetric trimers will assume a terminal velocity at an angle with respect to the external flow. For these particles, the interactions with the side walls become important eventually, as this forces the particles (for certain disk size ratios R_1/R_3) to move parallel to the sidewalls at an orientation that differs from the analytically predicted value.

These results provide a further step towards engineering the particle motion in

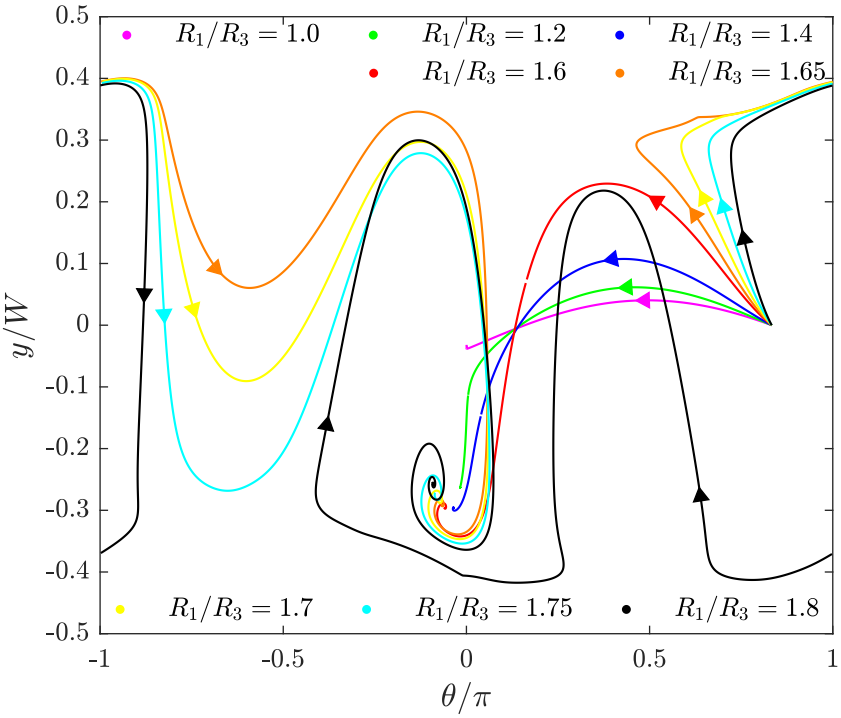

Figure 14: Particle trajectories in the (θ, y) phase space, where the direction of time is indicated by the arrows, for trimer particles with $R_2 = 2R_3 = 2H$ and varying $1 \leq R_1/R_3 \leq 1.8$. Initially, $\theta(0) = 5\pi/6$ and $y(0) = 0$ for every trimer particle.

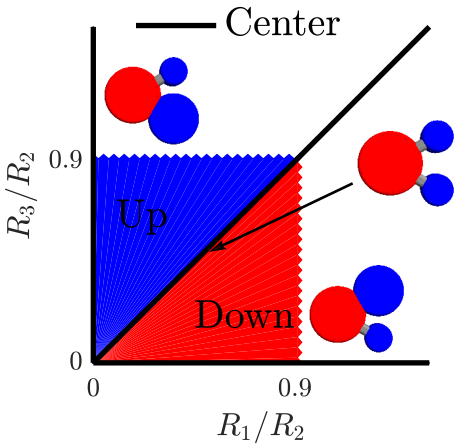

Figure 15: State diagram of the long-time y-position of trimer particles, consisting of three disks with radii R_i (R_2 corresponding to the middle disk) . The black lines indicate symmetric particles with $R_1 = R_2$ (symmetric trimers) and $R_1 = 0$ or $R_3 = 0$ (dimers), which move to the center of the channel. The red triangle indicates shapes that have a long-time y-position close to the lower boundary at $y = -W/2$, the blue triangle indicates shapes with a long-time y-position close to the upper boundary at $y = W/2$.

confined geometries. Our analytical results allow us to determine the particle trajectories by only calculating a few geometry-dependent quantities from numerical solutions of the Stokes (or Brinkman) equation. This in turn opens the door towards further tailoring the particle trajectories to any given demand or design by making use of optimisation schemes, e.g., genetic optimization algorithms [28].

In future research, it will be very interesting to further investigate the interaction with the sidewalls. Specifically, we could further investigate the dependence of the (strength of) the side wall interaction on the particle geometry, and for which particle geometries this is possible (completing the state diagram in Fig. 15). In this way, we hope to discover a mechanism to engineer the asymptotic y-position of the particles in the channel, by further tuning the particle geometry, and thus making a step forward in designing self-steering particles. Moreover, comparison of our analysis and results with experiments is being pursued at the moment.

Acknowledgments

This work is part of the D-ITP consortium, a program of the Netherlands Organisation for Scientific Research (NWO) that is funded by the Dutch Ministry of Education, Culture and Science (OCW). We acknowledge financial support from an NWO-VICI grant. S.S. acknowledges funding from the European Union's Horizon 2020 programme under the Marie Skłodowska-Curie grant agreement No. 656327.

Appendix A. Detailed derivations

In this appendix, we present some of the explicit solutions and calculations.

Appendix A.1. Explicit derivation of the equation of motion and expressions for the timescales.

We can explicitly write out the equations of motion (1) as

$$\begin{aligned}\begin{pmatrix} 0 \\ 0 \\ 0 \end{pmatrix} &= -\begin{pmatrix} R_{11} & R_{12} & R_{13} \\ R_{12} & R_{22} & R_{23} \\ R_{13} & R_{23} & R_{33} \end{pmatrix}\begin{pmatrix} U'_{p,x} \\ U'_{p,y} \\ \omega_p \end{pmatrix} \\ &\quad + \begin{pmatrix} R_{0,11} & R_{0,12} \\ R_{0,21} & R_{0,22} \\ R_{0,31} & R_{0,32} \end{pmatrix}\begin{pmatrix} U'_{0,x} \\ U'_{0,y} \end{pmatrix} \qquad \text{(A.1)} \\ &= -\begin{pmatrix} R_{11} & R_{12} & R_{13} \\ R_{12} & R_{22} & R_{23} \\ R_{13} & R_{23} & R_{33} \end{pmatrix}\begin{pmatrix} U_{p,x}\cos\theta + U_{p,y}\sin\theta \\ -U_{p,x}\sin\theta + U_{p,y}\cos\theta \\ \omega_p \end{pmatrix} \\ &\quad + \begin{pmatrix} R_{0,11} & R_{0,12} \\ R_{0,21} & R_{0,22} \\ R_{0,31} & R_{0,32} \end{pmatrix}\begin{pmatrix} U_0\cos\theta \\ -U_0\sin\theta \end{pmatrix}, \qquad \text{(A.2)}\end{aligned}$$

where the primed and unprimed velocities are with respect to the particle and channel frame coordinates, respectively. We solve this linear equation to obtain the velocities $U_{p,x}, U_{p,y}$ and ω_p. Solving this equation for $\omega_p \equiv \dot{\theta}$, gives

$$\dot{\theta} = \frac{1}{\tau_1}\sin\theta + \frac{1}{\tau_2}\cos\theta, \qquad \text{(A.3)}$$

where the timescales τ_1 and τ_2 are given by

$$\begin{aligned}\tau_1^{-1} &= U_0\Big(- R_{0,32}R_{12}^2 + R_{0,22}R_{12}R_{13} + R_{0,32}R_{11}R_{22} \\ &\quad - R_{0,12}R_{13}R_{22} - R_{0,22}R_{11}R_{23} + R_{0,12}R_{12}R_{23}\Big)\times \\ &\quad \Big(R_{13}^2R_{22} - 2R_{12}R_{13}R_{23} + R_{12}^2R_{33} + R_{11}(R_{23}^2 - R_{22}R_{33})\Big)^{-1}, \qquad \text{(A.4)} \\ \tau_2^{-1} &= U_0\Big(- R_{0,21}R_{12}R_{13} + R_{0,11}R_{13}R_{22} + R_{0,31}R_{12}^2 \\ &\quad - R_{0,31}R_{11}R_{22} + R_{0,21}R_{11}R_{23} - R_{0,11}R_{12}R_{23}\Big)\times \\ &\quad \Big(R_{13}^2R_{22} - 2R_{12}R_{13}R_{23} + R_{12}^2R_{33} + R_{11}(R_{23}^2 - R_{22}R_{33})\Big)^{-1}. \qquad \text{(A.5)}\end{aligned}$$

Next, we solve Eq. (A.2) for the transversal velocity $U_{p,y} \equiv \dot{y}$, which results in

$$\frac{\dot{y}}{H} = \frac{1}{\tau_{y,1}}\sin^2\theta + \frac{1}{\tau_{y,2}}\sin\theta\cos\theta + \frac{1}{\tau_{y,3}}\cos^2\theta, \qquad \text{(A.6)}$$

with timescales $\tau_{y,i}(i=1,2,3)$ given by

$$\tau_{y,1} = U_0 C^{-1}\Big\{ - R_{0,32}R_{13}R_{22} + R_{0,32}R_{12}R_{23} + R_{0,22}R_{13}R_{23} - R_{0,12}R_{23}^2 - R_{0,22}R_{12}R_{33} + R_{0,12}R_{22}R_{33}\Big\}, \tag{A.7}$$

$$\begin{aligned}\tau_{y,2} = U_0 C^{-1}\Big\{ & R_{0,32}R_{12}R_{13} - R_{0,22}R_{13}^2 + R_{0,31}R_{13}R_{22} \\ & - R_{0,32}R_{11}R_{23} - R_{0,31}R_{12}R_{23} + R_{0,12}R_{13}R_{23} \\ & - R_{0,21}R_{13}R_{23} + R_{0,11}R_{23}^2 + R_{0,22}R_{11}R_{33} \\ & - R_{0,12}R_{12}R_{33} + R_{0,21}R_{12}R_{33} - R_{0,11}R_{22}R_{33}\Big\},\end{aligned} \tag{A.8}$$

$$\tau_{y,3} = U_0 C^{-1}\Big\{ - R_{0,31}R_{12}R_{13} + R_{0,21}R_{13}^2 + R_{0,31}R_{11}R_{23} - R_{0,11}R_{13}R_{23} - R_{0,21}R_{11}R_{33} + R_{0,11}R_{12}R_{33}\Big\}, \tag{A.9}$$

$$C = \Big(R_{13}^2R_{22} - 2R_{12}R_{13}R_{23} + R_{12}^2R_{33} + R_{11}(R_{23}^2 - R_{22}R_{33})\Big). \tag{A.10}$$

Appendix A.2. Analytic solution of the angular equation

In this section, we derive the analytical solution (6) of Eq. (4). We can separate the variables to find

$$\sqrt{\left(\frac{1}{\tau_1}\right)^2 + \left(\frac{1}{\tau_2}\right)^2}\int_0^t dt' = \sqrt{\left(\frac{1}{\tau_1}\right)^2 + \left(\frac{1}{\tau_2}\right)^2}\, t \tag{A.11}$$

$$= \int_{\theta_0}^{\theta} \frac{d\theta'}{\sin(\theta'+\Delta)} = \int_{\theta_0+\Delta}^{\theta+\Delta} \frac{d\theta''}{\sin\theta''} \tag{A.12}$$

Next, we use the famous tangent half-angle substitution, $x = \tan(\theta/2)$, which allows us to write the Jacobian and the trigonometric functions as

$$d\theta = \frac{2dx}{1+x^2}, \quad \sin\theta = \frac{2x}{1+x^2}, \quad \cos\theta = \frac{1-x^2}{1+x^2}. \tag{A.13}$$

Plugging this in, we find

$$\sqrt{\left(\frac{1}{\tau_1}\right)^2 + \left(\frac{1}{\tau_2}\right)^2}\, t = \int_{x_0}^{x} \frac{dx'}{x} = \log x - \log x_0 \tag{A.14}$$

$$= \log\tan\frac{\theta+\Delta}{2} - \log\tan\frac{\theta_0+\Delta}{2}. \tag{A.15}$$

We invert this relation to find

$$\theta(t) = -\Delta + 2\arctan\left[\tan\left(\frac{\theta_0+\Delta}{2}\right)\exp\left(t\sqrt{\tau_1^{-2}+\tau_2^{-2}}\right)\right]. \tag{A.16}$$

Appendix A.3. Integration and further analysis of the transversal motion in the mirror symmetric case

Knowing the solution (A.16) for θ, we can proceed to solve Eq. (15) for the transversal motion:

$$\dot{y}/H = \frac{-1}{\tau_y}\sin\left(4\arctan\left[\tan\frac{\theta_0}{2}\ e^{-t/\tau}\right]\right), \quad y(0)/H = 0. \tag{A.17}$$

To integrate, we use double angle formulas for the sine and consine and that

$$\sin(\arctan(x)) = \frac{x}{\sqrt{1+x^2}}, \quad \cos(\arctan x) = \frac{1}{\sqrt{1+x^2}}. \tag{A.18}$$

Applying the double angle formulas twice, we obtain

$$\begin{aligned}\sin(4\arctan z) &= 4\sin(\arctan z)\cos(\arctan z) \\ &\quad\times\left(\cos^2(\arctan z) - \sin^2(\arctan z)\right) &\text{(A.19)}\\ &= 4\frac{z}{\sqrt{1+z^2}}\frac{1}{\sqrt{1+z^2}}\Big(\frac{1}{1+z^2} - \frac{z^2}{1+z^2}\Big) = \frac{4z(1-z^2)}{(1+z^2)^2} &\text{(A.20)}\end{aligned}$$

Next, abbreviating $\tan(\theta_0/2) = \alpha$ and leaving the integration boundaries for a moment, we can integrate:

$$\begin{aligned}\int dt U_y(t) &= \frac{-\tau}{\tau_y}\int dt' \sin\left(4\arctan\left[\alpha\ e^{-t'}\right]\right) &\text{(A.21)}\\ &= \frac{-4\tau}{\tau_y}\int dt' \frac{\alpha e^{-t'}(1-\alpha^2 e^{-2t'})}{(1+\alpha^2 e^{-2t'})^2} &\text{(A.22)}\\ &= \frac{4\tau}{\tau_y}\int dq \frac{1-q^2}{(1+q^2)^2} \quad (q = \alpha e^{-t}, dq = -\alpha e^{-t}dt) &\text{(A.23)}\\ &= \frac{4\tau}{\tau_y}\frac{q}{1+q^2} = \frac{4\tau}{\tau_y}\frac{\alpha e^{-t/\tau}}{1+\alpha^2 e^{-2t/\tau}} = \frac{4\tau}{\tau_y}\frac{\alpha e^{t/\tau}}{\alpha^2 + e^{2t/\tau}}. &\text{(A.24)}\end{aligned}$$

Now, we reenter $\alpha = \tan(\theta_0/2) = \sin\theta_0/(1+\cos\theta_0)$:

$$\begin{aligned}\int dt U_y(t) &= \frac{4\tau}{\tau_y}\frac{\tan\theta_0/2 e^{t/\tau}}{\tan^2\theta_0/2 + e^{2t/\tau}} = \frac{4\tau}{\tau_y}\frac{\sin\theta_0 e^{t/\tau}}{\frac{\sin^2\theta_0}{1+\cos\theta_0} + (1+\cos\theta_0)e^{2t/\tau}} &\text{(A.25)}\\ &= \frac{4\tau}{\tau_y}\frac{\sin\theta_0 e^{t/\tau}}{(1-\cos\theta_0) + (1+\cos\theta_0)e^{2t/\tau}} &\text{(A.26)}\\ &= \frac{4\tau}{\tau_y}\frac{\sin\theta_0 e^{t/\tau}}{(1+e^{2t/\tau}) + (e^{2t/\tau}-1)\cos\theta_0} &\text{(A.27)}\\ &= \frac{2\tau}{\tau_y}\frac{\sin\theta_0}{\cosh(t/\tau) + \sinh(t/\tau)\cos\theta_0}. &\text{(A.28)}\end{aligned}$$

Requiring that $y(t=0) = 0$, we find:

$$y(t)/H = \frac{2\tau\sin\theta_0}{\tau_y}\left(\frac{1}{\cosh(t/\tau) + \sinh(t/\tau)\cos\theta_0} - 1\right). \tag{A.29}$$

Note that although we have derived this solution for the case of a minus sign in Eq. (11), the solution corresponding to the opposite sign can, as before, be obtained by simply substituting $\tau \to -\tau$.

To determine whether the time at crossing $y = 0$ agrees between the analytical solution and the numerically calculated trajectories, we calculate the time t_c at which $y = 0$: setting $y(t_c) = 0$ leads to

$$\cosh(t/\tau) + \sinh(t/\tau)\cos\theta_0 = 1 \tag{A.30}$$

$$\to \quad t/\tau = \log\frac{1 \pm \cos\theta_0}{1 + \cos\theta_0} \tag{A.31}$$

$$\to \quad t/\tau = 0 \quad \vee \quad t/\tau = \log\frac{1 - \cos\theta_0}{1 + \cos\theta_0}. \tag{A.32}$$

We can also find the position of the maximum, by setting the velocity to zero:

$$0 = \sin\left(4\arctan\left[\tan\frac{\theta_0}{2}\, e^{-t/\tau}\right]\right) \to \tan\frac{\theta_0}{2}\, e^{-t/\tau} = \tan\frac{k\pi}{4}, k \in \mathbb{Z}. \tag{A.33}$$

Since the lefthand side is positive for $0 < \theta_0 < \pi$, we see that the $k = 4l, l \in \mathbb{Z}$ solutions correspond to the asymptote $t \to \infty$, while the other solution gives us the maximum

$$t_m/\tau = \log\left(\tan\frac{\theta_0}{2}\right) = \log\left(\frac{\sin\theta_0}{1 + \cos\theta_0}\right) = \frac{1}{2}\log\left(\frac{\sin^2\theta_0}{(1 + \cos\theta_0)^2}\right) \tag{A.34}$$

$$= \frac{1}{2}\log\left(\frac{1 - \cos\theta_0}{1 + \cos\theta_0}\right) = \frac{t_c/\tau}{2}, \tag{A.35}$$

Note that this actually requires $\pi/2 < \theta_0 < \pi$. For $0 < \theta_0 < \pi/2$, there is no maximum. For $\pi/2 < \theta_0 < \pi$, the height of the peak is given by

$$y(t_m)/H = \tag{A.36}$$

$$\frac{2\tau\sin\theta_0}{\tau_y}\left(\frac{1}{\cosh(t_m/\tau) + \sinh(t_m/\tau)\cos\theta_0} - 1\right) \tag{A.37}$$

$$= \frac{2\tau\sin\theta_0}{\tau_y}\left(\frac{2}{\left(\sqrt{\frac{1-\cos\theta_0}{1+\cos\theta_0}} + \sqrt{\frac{1+\cos\theta_0}{1-\cos\theta_0}}\right) + \cos\theta_0\left(\sqrt{\frac{1-\cos\theta_0}{1+\cos\theta_0}} - \sqrt{\frac{1+\cos\theta_0}{1-\cos\theta_0}}\right)} - 1\right) \tag{A.38}$$

$$= \frac{2\tau\sin\theta_0}{\tau_y}\left(\frac{2\sqrt{1 + \cos\theta_0}\sqrt{1 - \cos\theta_0}}{(1 - \cos\theta_0) + (1 + \cos\theta_0) + \cos\theta_0(1 - \cos\theta_0) - (1 + \cos\theta_0)}\right) \tag{A.39}$$

$$= \frac{2\tau\sin\theta_0}{\tau_y}\left(\frac{2\sin\theta}{2 - 2\cos^2\theta_0} - 1\right) = \frac{2\tau}{\tau_y}(1 - \sin\theta_0) \tag{A.40}$$

Finally, we observe that $\theta(t_m) = \pi/2$, which follows directly from the fact that the right-hand-side of (15) changes sign for $\theta = \pi/2$. Alternatively, setting $\theta = \pi/2$ in Eq. 13 and solving for t, will result in an equation identical to Eq. (A.33).

Appendix B. Supplementary material: animations

Animations that support this work, as well as descriptions of these animations, can be found at `http://web.science.uu.nl/itf/brambet.htm`.

References

[1] Oakey J, Applegate Jr R W, Arellano E, Carlo D D, Graves S W and Toner M 2010 *Analytical chemistry* **82** 3862–3867

[2] Wang L, Flanagan L A, Jeon N L, Monuki E and Lee A P 2007 *Lab on a Chip* **7** 1114–1120

[3] Mao X, Lin S C S, Dong C and Huang T J 2009 *Lab on a Chip* **9** 1583–1589

[4] Gossett D R, Weaver W M, Mach A J, Hur S C, Tse H T K, Lee W, Amini H and Di Carlo D 2010 *Analytical and bioanalytical chemistry* **397** 3249–3267

[5] Tewhey R, Warner J B, Nakano M, Libby B, Medkova M, David P H, Kotsopoulos S K, Samuels M L, Hutchison J B, Larson J W *et al.* 2009 *Nature biotechnology* **27** 1025–1031

[6] Toner M and Irimia D 2005 *Annu. Rev. Biomed. Eng.* **7** 77–103

[7] Xuan X, Zhu J and Church C 2010 *Microfluidics and nanofluidics* **9** 1–16

[8] Sajeesh P and Sen A K 2014 *Microfluidics and nanofluidics* **17** 1–52

[9] Pamme N 2007 *Lab on a Chip* **7** 1644–1659

[10] Zeming K K, Ranjan S and Zhang Y 2013 *Nature communications* **4** 1625

[11] Li W, Yan S, Sluyter R, Nguyen N T, Zhang J and Alici G 2014 *Scientific Reports*

[12] Jeon H, Kim Y and Lim G 2016 *Scientific reports* **6**

[13] Masaeli M, Sollier E, Amini H, Mao W, Camacho K, Doshi N, Mitragotri S, Alexeev A and Di Carlo D 2012 *Physical Review X* **2** 031017

[14] Uspal W E and Doyle P S 2012 *Physical Review E* **85** 016325

[15] Uspal W E, Eral H B and Doyle P S 2013 *Nature communications* **4**

[16] Berthet H, Fermigier M and Lindner A 2013 *Physics of Fluids* **25** 103601

[17] Dendukuri D, Pregibon D C, Collins J, Hatton T A and Doyle P S 2006 *Nature materials* **5** 365–369

[18] Bet B, Georgiev R, Uspal W, Eral H B, van Roij R and Samin S 2017 *arXiv preprint arXiv:1710.04561*

[19] Staben M E, Zinchenko A Z and Davis R H 2003 *physics of fluids* **15** 1711–1733

[20] Pozrikidis C 1994 *Journal of Fluid Mechanics* **261** 199–222

[21] Kim S and Karrila S *1991, Microhydrodynamics: Principles and Selected Applications, Butterworth-Heinemann, Boston*

[22] Happel J and Brenner H 2012 *Low Reynolds number hydrodynamics: with special applications to particulate media* vol 1 (Springer Science & Business Media)

[23] Dhont J 1996 *An Introduction to Dynamics of Colloids* (Elsevier)

[24] Leal L G 2007 *Advanced transport phenomena: fluid mechanics and convective transport processes* (Cambridge University Press)

[25] Guazzelli E and Morris J F 2011 *A physical introduction to suspension dynamics* vol 45 (Cambridge University Press)

[26] Brinkman H 1949 *Applied Scientific Research* **1** 27–34

[27] Uspal W E and Doyle P S 2014 *Soft matter* **10** 5177–5191

[28] Charbonneau P 2002 *NCAR Technical Note* 74